

# Cytotoxicity and *in Vitro* Degradation Kinetics of Foundry-Compatible Semiconductor Nanomembranes and Electronic Microcomponents

Jan-Kai Chang,<sup>†,¶</sup> M. A. Bashar Emon,<sup>‡,¶</sup> Chia-Shuo Li,<sup>§</sup> Quansan Yang,<sup>†,¶</sup> Hui-Ping Chang,<sup>§,⊥</sup> Zijian Yang,<sup>⊥</sup> Chih-I Wu,<sup>§</sup> M. Taher Saif,<sup>\*,‡</sup> and John A. Rogers<sup>\*,†,⊥,#</sup>

<sup>†</sup>Center for Bio-Integrated Electronics, Northwestern University, Evanston, Illinois 60208, United States

<sup>‡</sup>Department of Mechanical Science and Engineering, University of Illinois at Urbana–Champaign, Urbana, Illinois 61801, United States

<sup>§</sup>Graduate Institute of Photonics and Optoelectronics, National Taiwan University, Taipei 10617, Taiwan

<sup>¶</sup>Department of Mechanical Engineering, Northwestern University, Evanston, Illinois 60208, United States

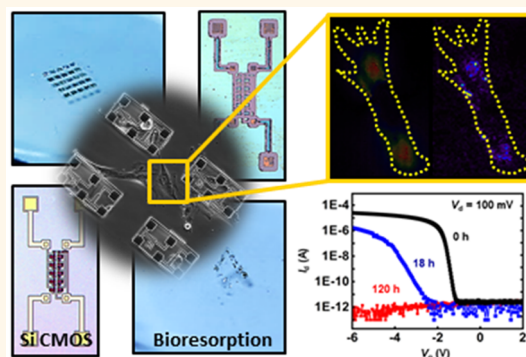
<sup>⊥</sup>Frederick Seitz Materials Research Laboratory, University of Illinois at Urbana–Champaign, Urbana, Illinois 61801, United States

<sup>#</sup>Departments of Materials Science and Engineering, Biomedical Engineering, Neurological Surgery, Chemistry, Mechanical Engineering, Electrical Engineering and Computer Science, Simpson Querrey Institute for BioNanotechnology, McCormick School of Engineering, and Feinberg School of Medicine, Northwestern University, Evanston, Illinois 60208, United States

## Supporting Information

**ABSTRACT:** Foundry-compatible materials and processing approaches serve as the foundations for advanced, active implantable microsystems that can dissolve in biofluids into biocompatible reaction products, with broad potential applications in biomedicine. The results reported here include *in vitro* studies of the dissolution kinetics and nanoscale bioresorption behaviors of device-grade thin films of Si, SiN<sub>x</sub>, SiO<sub>2</sub>, and W in the presence of dynamic cell cultures *via* atomic force microscopy and X-ray photoemission spectroscopy. *In situ* investigations of cell–extracellular mechanotransduction induced by cellular traction provide insights into the cytotoxicity of these same materials and of microcomponents formed with them using foundry-compatible processes, indicating potential cytotoxicity elicited by W at concentrations greater than 6 mM. The findings are of central relevance to the biocompatibility of modern Si-based electronics technologies as active, bioresorbable microsystems that interface with living tissues.

**KEYWORDS:** toxicity, bioresorption, implantable electronics, cell traction force, cell metabolism



Electronics technologies that decompose, degrade, and/or bioresorb in a controlled, timed fashion are of considerable interest due to their ability to serve as the basis for bioresorbable diagnostic and therapeutic implants. Advanced strategies in fabrication allow devices that function on time scales matched to a natural biological process, such as wound healing, and then disappear naturally without the need for retrieval.<sup>1–3</sup> Such types of physically transient devices are designed to fully bioresorb into their surroundings on predictable, engineered time scales, where constituent materials and device layouts define resorbable characteristics and associated dissolution kinetics.<sup>4–6</sup> Reported examples of material options include specially formulated organic materials

(*e.g.*, hygroscopic polymers, cellulose-based biomaterials), certain conventional metals and their alloys (*e.g.*, W, Mg, Mg alloys), and high-quality semiconductor/dielectric nanomembranes (*e.g.*, Si, ZnO, SiN<sub>x</sub>, SiO<sub>2</sub>).<sup>7–12</sup> Of the various bioresorbable materials that have been employed in transient electronics systems, inorganic semiconductors/dielectrics are of particular interest owing to their capacity to support high-performance operation with device designs aligned to those of

**Received:** June 13, 2018

**Accepted:** August 29, 2018

**Published:** August 30, 2018

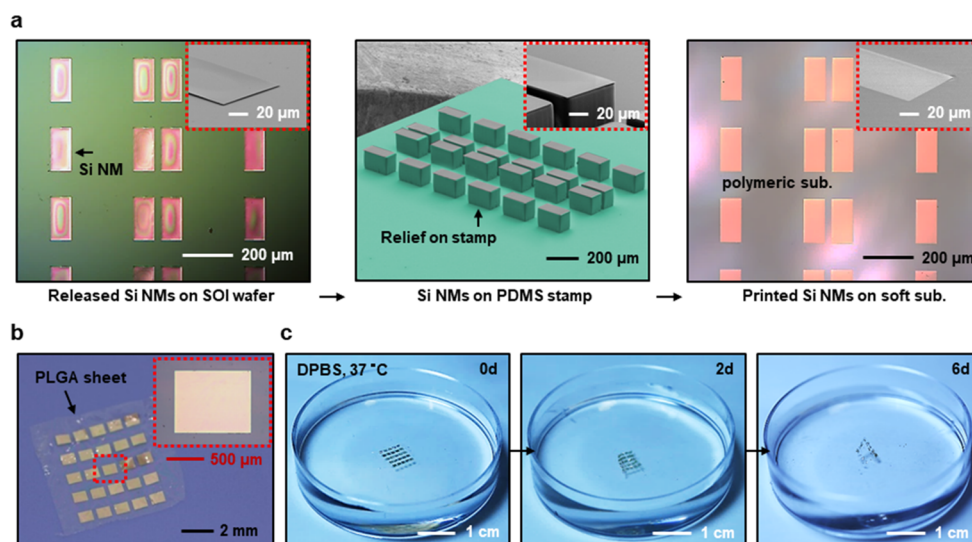


**Figure 1.** Transfer printing of Si NMs from SOI source wafers to soft, bioresorbable substrates. (a) Optical and SEM images of Si NMs (200 nm thick,  $80\ \mu\text{m} \times 160\ \mu\text{m}$ ) released from an SOI wafer, retrieved onto a PDMS stamp, and printed onto a polymeric substrate. The insets provide magnified views of a representative Si NM. The colored region corresponds to the stamp (cyan). (b) Photograph of arrays of Si NMs on a sheet of PLGA. The inset magnified view shows a representative  $0.8\ \text{mm} \times 1\ \text{mm}$  Si NM. (c) Images collected at several stages of dissolution of these Si NMs upon immersion in DPBS ( $1\times$ ,  $\text{pH}\ 7.0 \pm 0.1$ ) at physiological temperature ( $37\ ^\circ\text{C}$ ).

conventional complementary metal-oxide-semiconductor (CMOS) technologies.<sup>13–15</sup> An important consequence is the ability to form temporary bioelectronic implants into state-of-the-art modules with multifunctional modes of operation, as biomedical technologies for nerve interfaces, temporary cardiac and intracranial implants, and programmable drug delivery vehicles for monitoring, therapeutics, and infection mitigation.<sup>1,2,16–18</sup>

Rapid assessments of the biocompatibility of candidate materials and device architectures, in particular those that leverage foundry-compatible approaches, are critically important. In addition to *in vitro* studies of the chemistry of hydrolysis of metals,<sup>3–5</sup> insulators,<sup>6</sup> and semiconductor materials,<sup>7</sup> recent work demonstrates that Si-based bioresorbable microsystems can not only support sensory functions but also work actively to modulate biological processes *in vivo*.<sup>2</sup> Additional research identifies various material parameters that can affect biological responses, including size/shape, surface functionalization, crystallinity, and wettability, each with associated influence on dissolution kinetics and toxicity.<sup>19–24</sup> Nevertheless, the influence of device-grade electronic materials, and devices built with them, on living model biosystems remains unclear, particularly for systems derived from foundry-based manufacturing schemes. Specifically, cellular responses elicited by the high-quality, bioresorbable electronic components and the products of their dissolution have been examined only *via* simple cell viability assays and animal level histological studies. The results do not yield direct insights into cell metabolic activity, nor do they provide information on the dynamic reciprocity between the cell and extracellular microenvironment.<sup>25–28</sup>

The studies described here focus on *in vitro* dissolution of foundry-sourced Si,  $\text{SiO}_2$ ,  $\text{SiN}_x$ , and W thin film materials in the presence of cells and culture environment. The work includes *in situ* microscopic studies to examine the cellular responses to extracellular cues elicited by the bioresorbable electronics upon cell metabolism for cytotoxicity evaluation. Spectroscopic and microscopic investigations of these materials

reveal nanoscale bioresorption behaviors and chemistry at nanomembrane/biofluid interfaces, providing insights into associated bioactivity under physiological environments that mimic complex *in vivo* interactions. Analysis of mechano-transduction *via* traction force microscopy (TFM) offers *in vitro* platforms for direct monitoring of cell–extracellular matrix characteristics *in situ* during the culture of cells in the presence of foundry-compatible nanomembranes/microelectronics, revealing metabolic responses to the exposure of dissolution products upon material bioresorption. Such measurements of cellular activity serve as cell-based tests of biocompatibility and provide information on cytotoxicity for foundry-compatible materials in advanced bioresorbable implants.

## RESULTS AND DISCUSSION

Previous studies examined the hydrolysis of amorphous/porous silicon, lightly/heavily doped silicon, mono/polycrystalline silicon, and other silicon-based materials in biofluids and various aqueous solutions by microscopic imaging of patterned wafers and direct measurements of changes in thickness.<sup>8,13,27,29</sup> The dissolution chemistries involve a relatively simple reaction,  $\text{Si} + 4\text{H}_2\text{O} \rightarrow \text{Si}(\text{OH})_4 + 2\text{H}_2$ , although influenced in complex ways by chemical constituents in the surrounding aqueous environment. For a given temperature, the kinetics depend strongly on a collection of parameters, including pH, concentrations and types of dissolved ions, as well as the presence of reaction products and other chemicals in solution.<sup>8,26,29–31</sup> The time scales for complete dissolution of sheets of monocrystalline, device-grade Si (*i.e.*, silicon nanomembranes; Si NMs) at near-neutral pH in biofluids can be tuned from several hours to years, where dopant activation and surface oxidation provide the most important engineering control parameters.<sup>8,29</sup> Here, *in vitro* parametric investigations of the dissolution of device-grade Si NMs on bioresorbable polymer substrates establish essential aspects of the underlying chemical reactions and their role in determining the cytotoxicity of foundry-compatible electronic implants.

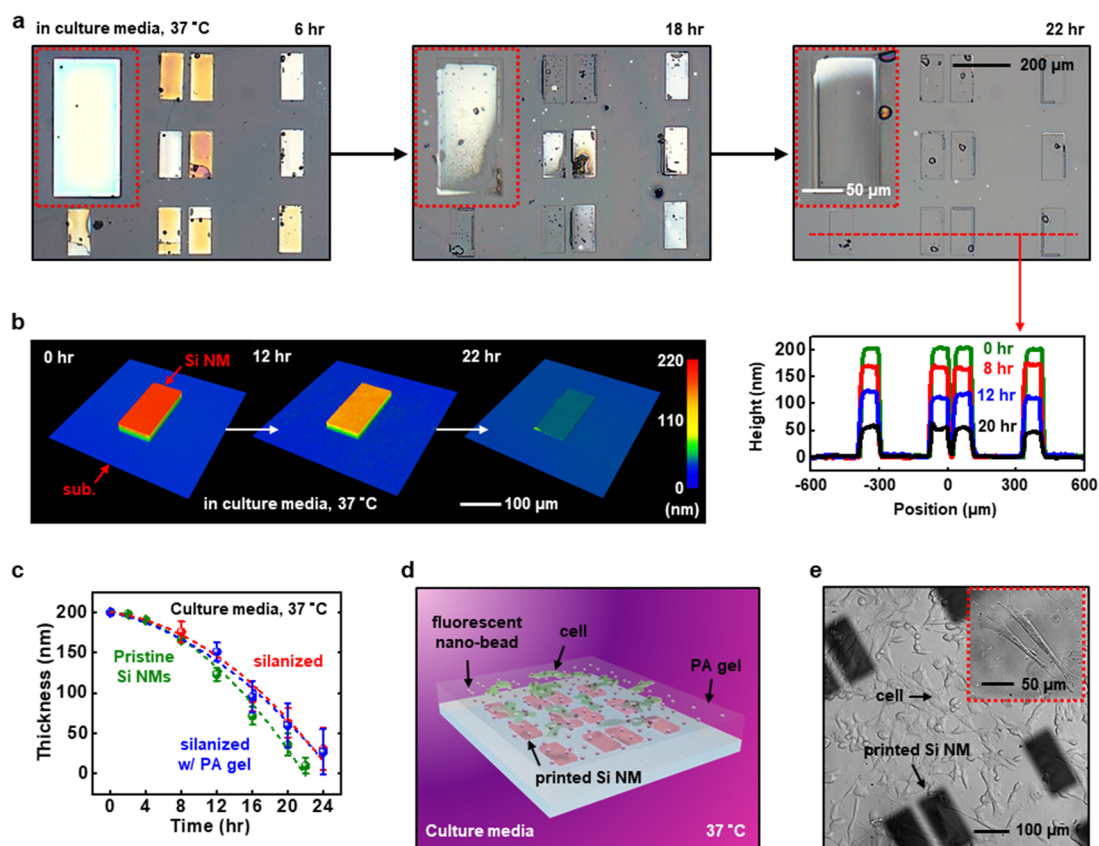


**Figure 2.** Dissolution kinetics of arrays of Si NMs in cell culture media. (a) Optical images with magnified views as insets for the evolution of the microstructure of Si NMs ( $80\ \mu\text{m} \times 160\ \mu\text{m}$ ) during dissolution. (b) Optical profilometry images and line scan profiles at different stages of dissolution. (c) Experimentally measured changes in thickness as a function of time for dissolution of Si NMs under various conditions. (d) Schematic illustration of a test structure for TFM characterization with cells cultured on arrays of Si NMs. (e) Phase-contrast images of arrays of Si NMs with an overcoat of PA gel, fluorescent nanobeads (not visible under current magnification), and adhered cells after 18 h.

Figure 1a illustrates the process of microscale assembly of Si NMs onto soft, bioresorbable materials at different stages of fabrication. Releasable arrays of Si NMs follow from processing of the top Si layer ( $\sim 200\ \text{nm}$ ) of silicon-on-insulator (SOI) wafers (SOITEC, France) by photolithography and reactive ion etching (RIE). Controlled undercut etching in hydrofluoric acid (HF) followed by photolithography yields supporting polymeric anchors for free-standing Si NMs that result from complete removal of buried oxide layer by further etching in HF. The structures formed in this way facilitate subsequent selective retrieval and transfer (*i.e.*, transfer printing with a micropatterned elastomeric stamp) onto foreign substrates. Details are in the Supporting Information (Figure S1) and the Experimental Section. Transferrable Si NMs in various sizes, shapes, geometries, and thicknesses follow naturally. An arrayed example of large Si NM platelets ( $0.8\ \text{mm} \times 1\ \text{mm}$ ) on a bioresorbable poly(lactic-co-glycolic acid) (PLGA) sheet appears in Figure 1b. The resulting structure undergoes hydrolysis upon immersion in Dulbecco's phosphate-buffered saline (DPBS) with pH, temperature, and osmolality aligned to physiological conditions, as shown in Figure 1c. The results indicate dissolution rates of  $25 \pm 3\ \text{nm/day}$  for printed Si NMs with doping levels of  $10^{15}\ \text{cm}^{-3}$  (p-Si, boron,  $14\text{--}18.9\ \Omega\text{-cm}$ ), with temporal and spatial uniformity during the dissolution process. These rates are slightly lower than those observed with standard PBS ( $35 \pm 1\ \text{nm/day}$ ), due mainly to the lack of Ca and Mg content but also with a possible minor influence of the sterile and nonpyrogenic environment of DPBS.

Although these evaluations yield valuable kinetic information, further investigations into the dissolution upon immersion in cell culture media are more directly relevant to bioresorption in biological environments. Figure 2 shows results for arrays of Si NMs in cell culture media at  $37\ ^\circ\text{C}$ . The media contain aqueous formulations of nutrients, antibiotics, and simulated plasma, with physiological levels of inorganic salts and protein albumin to ensure a stable active proliferation of mammalian cells and cell lines. The micrographs in Figure 2a highlight the exterior changes of Si NMs that occur as a result of degradation/dissolution. During dissolution, swelling of the polymeric substrate (PLGA in this case) occurs slowly in the first few hours of immersion, yielding stresses that can lead to fracture/disintegration of the supported Si NMs. Otherwise, changes in the thicknesses of the Si NMs monotonically follow the hydrolytic reactions between the Si NMs and the culture media, with a high level of microscopic uniformity across the spatial extent of each NM ( $80\ \mu\text{m} \times 160\ \mu\text{m}$ ). Time sequences of thickness measurements based on surface profilometry (Figure 2b) provide details, allowing parametric studies of the time scales for complete dissolution. The dissolution rate of printed Si NMs derived in this way suggests a nonlinear dependence on immersion time (green, Figure 2c), varying from  $2.1 \pm 0.5$  to  $12.8 \pm 2.3\ \text{nm/h}$ . This acceleration may follow from uncontrolled levels of natural degradation of the culture media *via* processes such as proteolysis, coagulation, and/or basification of the protein ingredients over time, perhaps as a consequence of the release of products of

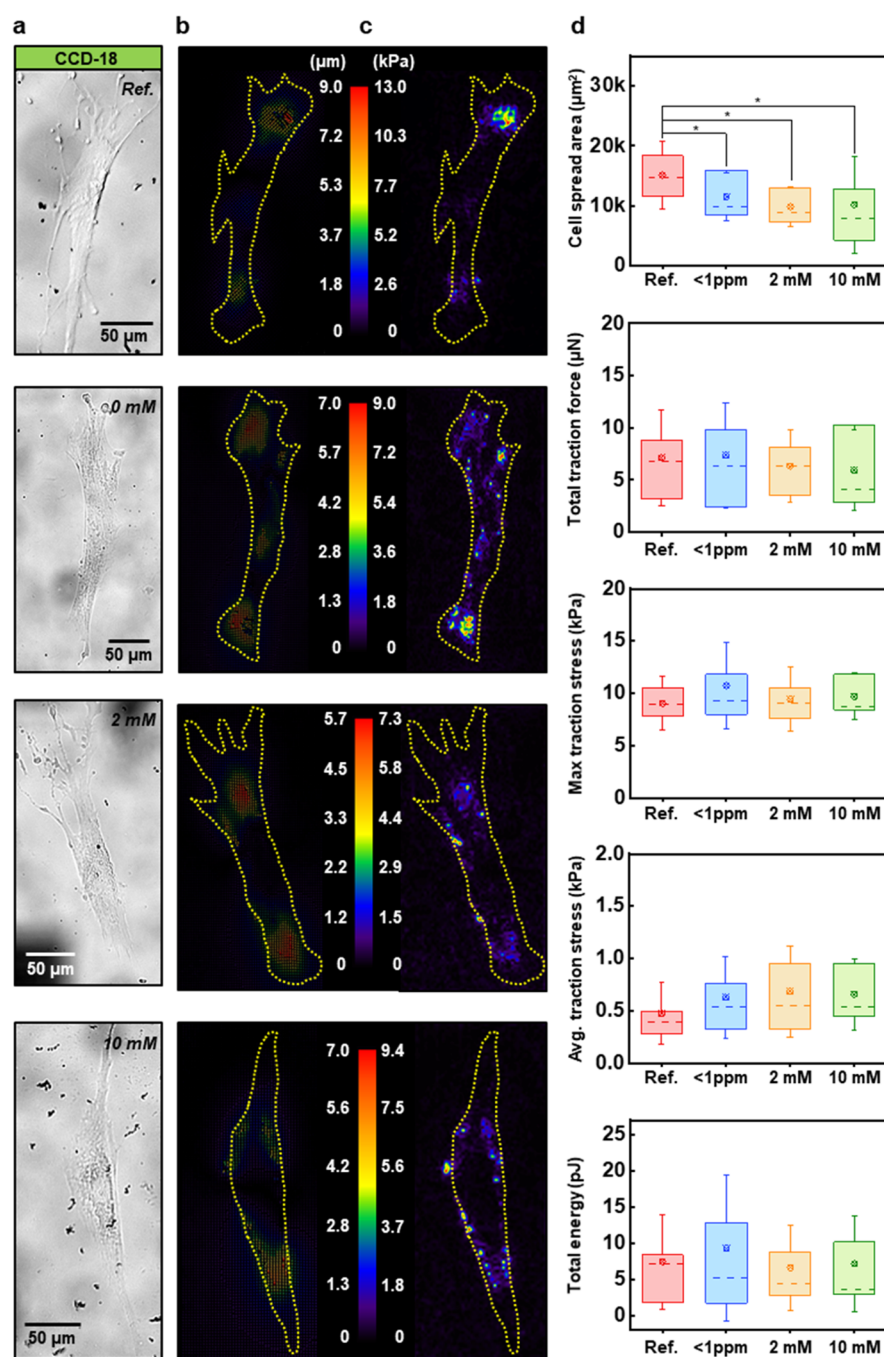


**Figure 3.** *In vitro* TFM evaluation of cytotoxicity associated with Si NMs and silicic acid. (a) Optical phase-contrast images of representative cells under cell culture media (Ref.), conditioned in the presence of Si NMs (<1 ppm), and dissolved in silicic acid at different concentrations (2 and 10 mM) after 18 h. (b) Vector plot of displacement fields underneath each of these same cells. (c) Traction stress maps derived from the results in (b). (d) Traction-associated properties of cells at the 18th hour as quantified from the live assay in (a). Significance of data variation was validated with two-sample *t*-test (*p*-value < 0.10 denoted by single asterisk).

dissolution and from the presence of oxygen from the ambient environment.<sup>32–35</sup> During the dissolution, Si converts into metasilicic acid ( $\text{H}_2\text{SiO}_3$ ), orthosilicic acid ( $\text{H}_4\text{SiO}_4$ ), disilicic acid ( $\text{H}_2\text{Si}_2\text{O}_5$ ), and pyrosilicic acid ( $\text{H}_6\text{Si}_2\text{O}_7$ ) upon reactions with the  $\text{OH}^-$  anion. These species may result in deprotonation of carbonate salt compositions that promote the release of cations and  $\text{CO}_2$ , leading to fast hydrolytic reactions as reported in previous studies on ionic strength and salinity.<sup>8,36,37</sup> A discussion of the surface chemistry of Si NMs after the reactive dissolution appears subsequently.

Similar results on the time dependence of dissolution for silanized Si NMs with (blue) and without (red) a coverage of poly(acrylamide) (PA) gel are also shown in Figure 2c for comparison. These common preculture treatments for cellular traction measurements slightly delay the dissolution *via* effects of surface passivation. Here, silanized Si NMs immobilize proteins due to the high reactivity of glutaraldehyde-activated surface toward amines, amides, and thiol groups in biomolecules, leading to enhanced adsorption of proteins/biomolecules that passivate the surfaces of the Si NMs at early

stages of dissolution.<sup>38</sup> The overlying PA gel ( $\sim 100\ \mu\text{m}$ ) may not significantly impede diffusive access of aqueous solution to the Si NMs due to its intrinsic permeability to water, as inferred by experimental observations of complete dissolution of embedded Si NMs after immersion for 24 h.

This finding supports the possibility for using this test structure, *i.e.*, arrays of Si NMs silanized and embedded beneath a film of PA gel, for *in situ* characterization of cell–extracellular matrix mechanotransduction. Such studies allow accurate determination of local cellular activity in response to silicon dissolution and associated cellular stimuli. Figure 2d presents a schematic diagram of the overall test structure for *in vitro* evaluations, with setups that incorporate a soft PA gel layer (modulus of  $\sim 5\ \text{kPa}$ ) above arrays of Si NMs on PLGA/glass substrates. Here, a random collection of fluorescent beads (diameters  $\sim 100\ \text{nm}$ ) infused within the gelant formulations at the same focal plane facilitates microscopic imaging. The transparency of the overall structure allows direct tracking of local deformations and stresses induced by cellular traction forces associated with cellular metabolic activity: increased cellular traction involves assembly of actin stress fibers and other anabolic processes determined by mechanosensitive set points, while a decrease of tension may initiate catabolic processes.<sup>39,40</sup> The overall structure for *in vitro* cell culture testing is shown in Figure 2e, where the phase-contrast images show mammalian cells adhered tightly to the PA gel coating on the Si NMs. This platform is effective for cell–extracellular matrix mechanotransduction and rapid, *in situ* assessment of cell activity by traction force microscopy.

Mechanotransduction due to cellular tractions follows from extracellular cues as responses to the culture microenvironment. In other words, the cells translate biological responses into mechanical information. Through TFM analysis, quantitative studies of cell spreading and traction forces in response to conditioned surroundings serve as foundations for understanding processes in cell migration, homeostasis, morphogenesis, wound healing, and other biological functions.<sup>41,42</sup> Here, *in vitro* assays of CCD18 human colon fibroblasts for TFM analysis (Figure 3) rely on experiments with conditioned cultures that include a control case (Ref.), a test structure with arrays of Si NMs ( $<1\ \text{ppm}$ ), and arrays of Si NMs with the addition of  $\text{Si}(\text{OH})_4$  extracts into the culture media (2 and 10 mM). The total Si content can be determined by calculating the amount of dissolved Si based on the weight loss and on direct experimental measurements by inductively coupled plasma optical emission spectrometry (ICP-OES). The ICP-OES analysis indicates that bioresorption of Si NMs releases Si into the media at concentrations of less than  $400\ \mu\text{g/L}$  throughout the *in vitro* culture and TFM characterization. Additional details and associated procedures are in the Experimental Section.

After conditioning the culture for 18 h, the area of cell spreading decreases with increasing  $\text{Si}(\text{OH})_4$  content in the surrounding microenvironment (Figure 3d). Other TFM parameters of stress, force, and strain energy show no apparent differences after 18 h of exposure to a maximum of 10 mM silicic acid in the culture environment, suggesting that biological activity related to adhesion and traction of the cells is not affected significantly at this dosage and time scale. Assays performed for further assessment of biocompatibility under each conditioned culture (Table 1) indicate a high viability of cells and their normal proliferation after exposure to the silicic acid stimuli, thereby supporting a lack of toxicity.

**Table 1. Cell Viability Calculated as the Fraction of Total Living Cells after Conditioning the Culture for 3, 9, and 18 h**

conditioned culture		time		
		3 h	9 h	18 h
		viable cells (%)	viable cells (%)	viable cells (%)
Si	2 mM	$102 \pm 3$	$104 \pm 1$	$103 \pm 1$
	10 mM	$98 \pm 1$	$98 \pm 1$	$99 \pm 4$
W	1.2 mM	$101 \pm 1$	$102 \pm 2$	$101 \pm 2$
	6 mM	$89 \pm 3$	$86 \pm 3$	$86 \pm 3$
electronics	0.01%	$99 \pm 3$	$100 \pm 1$	$100 \pm 3$

The results verify that device-grade silicon and its dissolution products are biologically safe, without measurable cytotoxic effects, consistent with extensive reports of bioavailable silicon in the nontoxic form of silicic acid and their use in biomedical engineering/medicine associated with bone mineralization, collagen synthesis, skin, hair, and nail health, atherosclerosis, Alzheimer's disease, immune system enhancement, and some other disorders or pharmacological effects.<sup>30,43–47</sup>

Unlike silicon and Si-based compounds that naturally resorb *via* metabolic reactions in a biocompatible manner, the toxicity of W is not well understood. Some reports describe that exposing multiple cultured human cells to significant levels of tungsten can result in local cytopathologic and subtle neurobehavioral effects,<sup>48–50</sup> while others suggest no chronic injuries, ill effects, or loss of function after consumption of 25–80 g of powdered tungsten metal.<sup>51–54</sup> Here, cell assays with W-conditioned culture and TFM analysis determine whether W in foundry-compatible formats or its degradation products, *i.e.*, tungstic acid in monohydrate and dihydrate forms of  $\text{WO}_3$ , interfere with cell metabolisms and/or elicit other biological processes. Figure 4 presents TFM results from representative cells under standard and W-conditioned culture (at concentrations of 1.2 and 6 mM) for 18 h. The displacement fields (Figure 4b) and traction stress maps (Figure 4c) of the same viable cells show changes in extracellular matrix as a measure of cell metabolic activity. As a result of exposure to tungstic acid, cells exhibit a significant decrease in their state of health and possibly metabolic activity, as maximum and average traction stresses decline with increasing W dissolution products in the surroundings (Figure 4d). Total force magnitudes and strain energies also decrease, although by small amounts, with increasing concentration of W dissolution products in the culture environment. The results are interpreted as a symptom of apoptosis since the reduction in traction force and focal adhesion may lead to the loss of cytoskeleton that is vital for cells to maintain nucleus structure/function and to survive *in vitro*. Similarly, results from viability tests (Table 1) reveal that an aggressive microenvironment with high concentrations of W degradation products surrounding the cells could have adverse effects on their viability, especially with prolonged exposure time. The results imply that high tungsten concentrations (6 mM in the form of the products of dissolution) may elicit local cytopathologic effects that eventually lead to apoptosis. Nevertheless, it is unlikely that at a given *in vitro* dissolution rate of  $154\ \mu\text{g/day/mm}^2$ , concentrations of W content will reach a level of toxicity in the human body, even locally, for the amounts of W used in electronics. For example, dissolution of a relatively large areal coverage of W (*i.e.*,  $80\ \mu\text{m} \times 80\ \mu\text{m}$  for a microcomponent of the sort described previously) would only

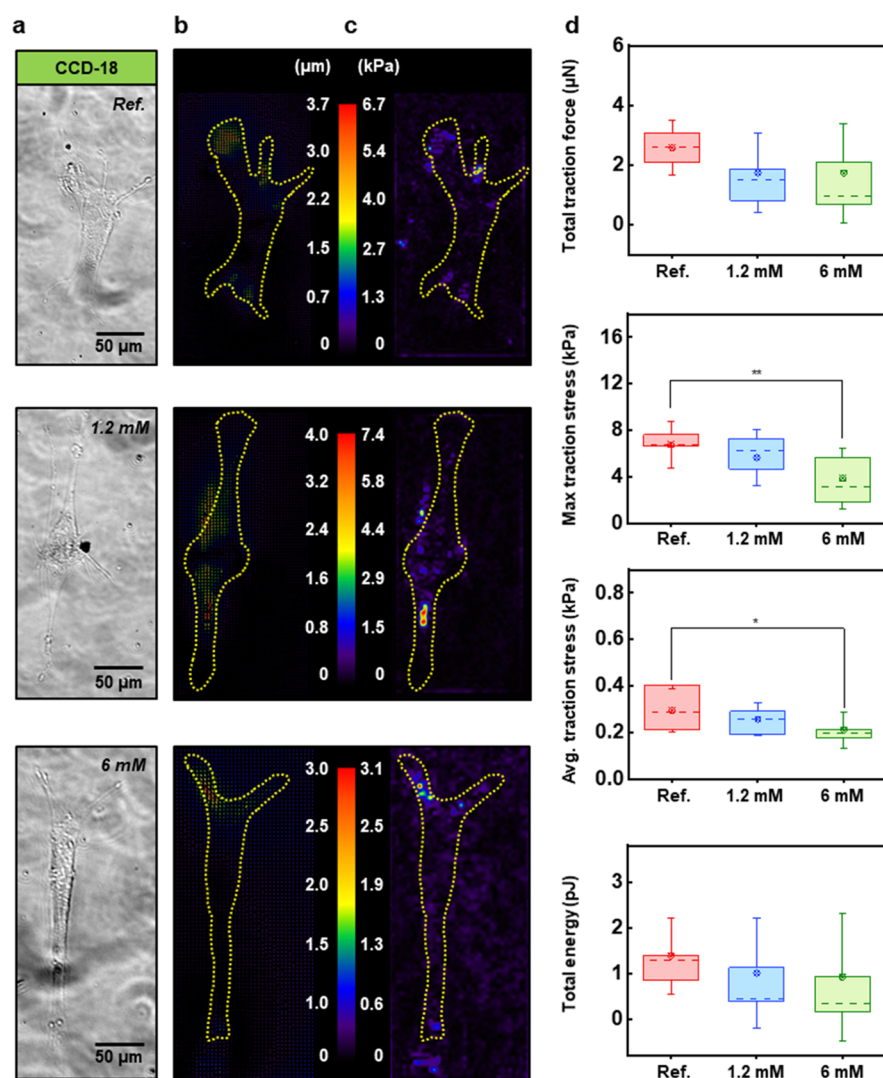


**Figure 4.** *In vitro* TFM evaluation of cytotoxicity associated with bioresorption products of W. (a) Optical phase-contrast images of representative cells under cell culture media (Ref.), conditioned with W dissolution at 1.2 and 6 mM after 18 h. (b) Vector plot of displacement fields underneath each of these same cells. (c) Traction stress maps derived from the results in (b). (d) Traction-associated properties of cells at the 18th hour as quantified from the live assay in (a). Significance of data variation was validated with two-sample *t*-test (*p*-value < 0.10 denoted by single asterisk, *p*-value < 0.05 denoted by double asterisk).

yield concentrations of 0.2 mM assuming a fixed volume of 1 mL of biofluids. More specifically, even if all of the W traces in a foundry-based 6 in. wafer dissolve in the human body (biofluid volume of ~40 L) without turnover of fluid *via* excretion/consumption, concentrations would only begin to reach levels (6.5 mM) with potential toxicity, as reported here.

Spectroscopic and microscopic methods allow further examination of the effects of *in vitro* bioresorption during cell metabolic activity, *via* surface characteristics of device-grade Si NMs, PECVD SiN<sub>x</sub>, thermally grown SiO<sub>2</sub>, and sputtered W after culture and proliferation of CCD18 human colon fibroblasts. Figure 5 highlights changes in chemical composition and nanoscale morphology after *in vitro* bioresorption for 5 days. X-ray photoelectron spectroscopy (XPS) reveals the surface chemistry of Si NMs and thin films of W, as shown in Figure 5a. The spectra indicate significant levels of biochemical residues adsorbed on surfaces (within 10 nm) that form the interfaces with cells in all cases, with strong peaks (normalized to Si or W signal depending on the test substrate) at 401.5 eV for nitrogen, at 347.0 and 350.55 eV for

calcium, and between 284.5 and 287.7 eV for carbon. These residues can be attributed to catabolic/metabolic products from cellular activity and/or natural nitrogen and carbon sources such as glutamine and pyruvate used during cell culture. Other chemistries from common ingredients such as inorganic salts (*e.g.*, MgSO<sub>4</sub>, NaHCO<sub>3</sub>, NaH<sub>2</sub>PO<sub>4</sub>, KCl) may also be present, although the photoemission signals are too weak to be observed. Depth profiling *via* monatomic argon ion beam milling of samples of partially bioresorbed Si and W reveals a decrement of valence states from the outer surface into the depth. The findings indicate that a mixture of oxides develops through the surface in contact with culture media/cells as the bioresorption proceeds. Due to the impermeability of monocrystalline Si,<sup>8</sup> the reactive processes occur only at the surface (within the 10 nm depth resolution of the XPS measurements), as inferred by the presence of the pristine Si 2p core level in the XPS spectra. Additional results based on Raman and Fourier-transform infrared spectroscopy confirm this surface-based process for bioresorption of Si NMs (Figure S2). Release of Si atoms into culture media is consistent with

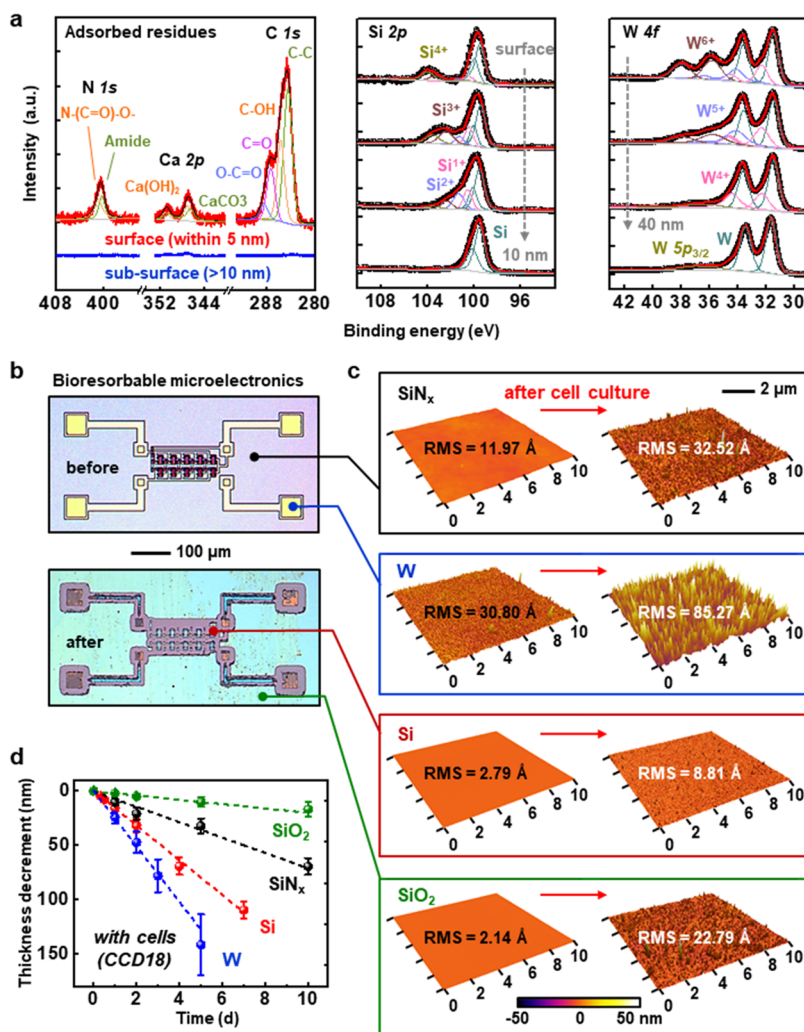


**Figure 5.** Characterization of surface chemistry and morphology associated with bioresorbable electronic microcomponents after *in vitro* cell culture. (a) XPS depth profiling of Si NMs and thin films of W after cell culture. (b) Optical images of bioresorbable microelectronic components consisting of Si, SiN<sub>x</sub>, SiO<sub>2</sub>, and W before and after bioresorption in culture media. (c) AFM morphological images of Si, SiN<sub>x</sub>, SiO<sub>2</sub>, and W before and after cell culture. (d) Calculated (dashed lines) and measured (symbols) changes in film thickness for Si, SiN<sub>x</sub>, SiO<sub>2</sub>, and W during cell culture over 10 days.

Si(OH)<sub>4</sub> products, where abundant biochemical residues and Si<sup>4+</sup> on the outermost surface of the Si appear in the XPS data. Sputtered W thin films, by comparison, have grain boundaries and micropores that enable liquid-phase diffusion of water and biomolecules. Continuous corrosion at the top surfaces and into the depth of the film occur in parallel, leading to a hybrid W–WO<sub>x</sub> coverage with a thickness greater than 40 nm after 5 days of culture, consistent with previous studies.<sup>55</sup> We note that preferential sputtering of oxygen over tungsten induced by ion beam milling may occur during the depth profiling but should not lead to a significant level of spectral variation upon sputtering for films with thicknesses in the range examined here.

Additional experiments to determine the effects of bioresorption on microstructure and nanoscale morphology involve atomic force microscopy (AFM) measurements on the same types of samples. Here, foundry-compatible microelectronic components constructed with these materials dissolve during cell culture (Figure 5b), in a fashion that follows the dissolution kinetics of the different constituent materials and the diffusivity of water throughout the multilayer

stacks. Figure 5c provides AFM images that highlight the changes in nanoscale morphology before and after cell culture, indicating increased surface roughness as a result of cell metabolic activity through biochemical reactions and/or bioresorption through hydrolysis of materials themselves. The enhanced roughness after cell culture likely follows from reactive diffusion, influenced by catalytic and other chemical effects of ions and surrounding biomolecules,<sup>56</sup> as observed in prior XPS results. The time-dependent changes in thickness determined by cross-sectional SEM images for these same materials in the presence of cell metabolic activity over 10 days appear in Figure 5d. The results are largely consistent with *in vitro* measurements of dissolution rates, with values that lie in a range comparable to that of previous studies for various types of aqueous solutions and biofluids,<sup>8,27,29</sup> with good levels of temporal and spatial uniformity at the macroscopic scale. Details of dissolution rates are summarized in Table 2. We note that the *in vitro* assays tested here represent the initial results of such dissolution kinetics/chemistries. Future work will explore the use of drug dissolution pharmacopoeia tests

**Table 2. Dissolution Rates of Si, SiN<sub>x</sub>, SiO<sub>2</sub>, and W during the Culture of CCD18 Fibroblasts**

dissolution rate (nm/d)	w/cells in CO <sub>2</sub> -filled incubator			
	Si	W	SiN <sub>x</sub>	SiO <sub>2</sub>
	16.1	25.4	7.1	2.0

(e.g., USP, BP) to evaluate release of dissolution products *in vivo*.

Microelectronic devices sourced from a commercial foundry (X-Fab Semiconductor Foundries) provide examples of Si, SiN<sub>x</sub>, SiO<sub>2</sub>, and W thin films in high-performance electronics with fully bioresorbable formats.<sup>14,57</sup> Figure 6a highlights microcomponents of p-channel metal-oxide-semiconductor field-effect transistors (MOSFETs) released from the supporting SOI wafer. A schematic exploded view illustration shows the detailed configurations of transistors that include films of Si, SiN<sub>x</sub>, SiO<sub>2</sub>, Ti/TiN, and W. The presence of the Ti/TiN adhesion layer (<0.1% content of a typical device) may not elicit significant cytotoxicity effects, as these materials are known to be biologically inert in biofluids.<sup>58,59</sup> Here, a test structure similar to that in Figure 2d but with arrays of transistors in this microcomponent format (Figure S3) allows *in vitro* studies of biocompatibility of the devices along with the

products of their dissolution during the transience. As shown in Figure 6b, CCD18 cells incubated on this type of test structure at 37 °C tend to adhere along structural features following previously reported topology effects.<sup>24</sup> After 18 h of culture, the transfer characteristics of the transistors degrade rapidly due primarily to the dissolution/bioresorption of exposed tungsten traces and ionic transport through sites of corrosion, on time scales comparable to previous findings in Figure 5d. Specifically, ions/radicals from the culture media or from metabolic products (mostly positive species such as Ca<sup>+</sup>) diffuse and accumulate within the multilayered micro-components, where they produce local potentials and associated biases at the gates of the transistor channels, thereby electrostatically inducing adverse effects on the transfer characteristics, most prominently as shifts in the threshold voltage. The transistor functionality and key characteristics such as threshold voltage, subthreshold swing, and saturation current degrade in a corresponding manner. After 120 h of culture, the transistors no longer exhibit useful switching characteristics, as a result of the disintegration of the W interconnects. The embedded Si active layers persist at this stage due to the relatively slow dissolution of overlying films of SiN<sub>x</sub> and SiO<sub>2</sub>.

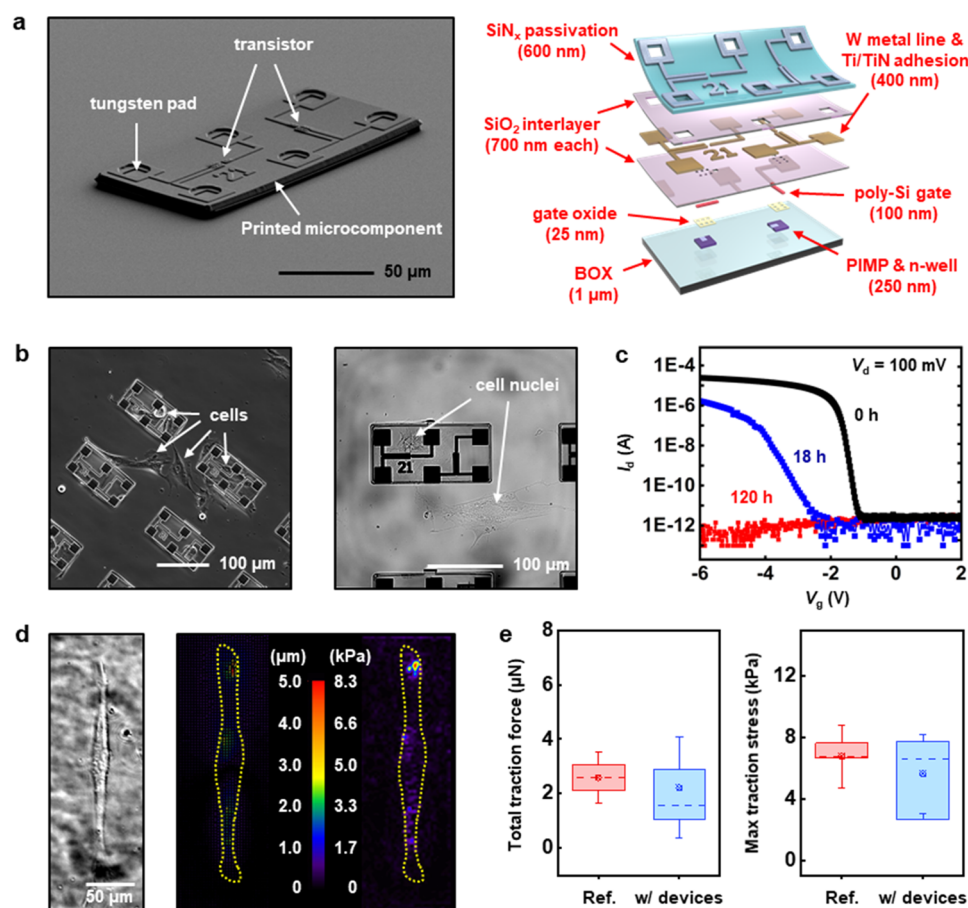


**Figure 6.** *In vitro* cell culture evaluations of cytotoxicity and performance degradation of bioresorbable transistors. (a) SEM image (left) and exploded view schematic illustration (right) of p-channel MOSFETs in microcomponent form and constructed with bioresorbable materials. (b) Phase-contrast images of arrays of such microcomponents with adhered cells over 18 h, corresponding to the stage of TFM characterization. (c) Transfer characteristics of a representative p-channel MOSFET before and after cell culture for 18 and 120 h. (d) TFM images of displacement and stress fields of a representative cell cultured on printed transistor arrays with conditioned media over 18 h. (e) Traction force and stress derived from the assay in (b).

Extracts of DPBS following partial device dissolution (some SiO<sub>2</sub> may remain) blended into culture media (~0.01 wt %) generate conditioned microenvironments for *in situ* mechanobiological studies of cell metabolic activity in response to the dissolved components (6.36 ppm for Si content and 78.3 ppm for W content by ICP-OES measurement). Cytotoxicity assays based on TFM characterizations (Figure 6d) determine the tonicity of CCD18 cells in such a conditioned microenvironment, as the traction-induced displacements of the extracellular matrix follow the metabolic reactions of cells to the surrounding stimuli. Figure 6e summarizes the generation of cellular traction forces under pristine (red, Ref.) and conditioned (blue, w/ devices) culture environments for 18 h, where no significant mechanobiological signs of apoptosis result from the presence of the devices or their dissolved components, compared to the control cases. Viability results for the same condition as shown in Table 1 also suggest the biocompatibility of these foundry-based forms of bioresorbable microelectronic components.

## CONCLUSION

The results presented here summarize findings from *in vitro* studies of bioresorption of device-grade Si, SiN<sub>x</sub>, SiO<sub>2</sub>, and W, as well as the effects of foundry-compatible electronic microcomponents on cell metabolism and viability. *In situ* mechanobiological investigations of cell metabolic activity that examine cell–extracellular matrix interactions reveal the dynamic reciprocity between cells, bioresorbable materials/devices, and the products of their dissolution, suggesting that dissolved components are biocompatible without significant cytotoxicity effects on the cells. The results demonstrate the feasibility of constructing biointerfaced electronic devices for use in temporary active biomedical devices that leverage conventional Si CMOS technologies for advanced modes of operation.

## EXPERIMENTAL SECTION

**Preparation of Test Structure.** Photolithography and RIE defined arrays of Si NMs (200 nm initial thickness) on SOI source wafers (SOITEC). Controlled HF etching removed the exposed buried oxide layer (1 μm) and partially undercut regions beneath the borders of the Si NMs. Applying an overcoat of photoresist (~2 μm; AZ5214), flood exposing to UV light, and performing a development process (AZ 917 MIF) yielded an anchor structure of underexposed photoresist in the undercut trenches. Additional exposure to UV light through the photomask used in the process of defining the Si NMs but aligned to be partially overlapped with the previously formed patterns created an entrance for HF after basic development. An additional immersion in HF removed the buried oxide under the Si NMs, thereby resulting in a free-standing configuration supported only by the photoresist at the perimeter regions.<sup>60</sup> A stamp of PDMS (10:1 mixture of base to curing agent) formed by the techniques of soft lithography allowed transfer printing of the Si NMs onto PLGA (85:15; Sigma-Aldrich)-coated glass substrates.<sup>61</sup> Immersion in acetone immediately after retrieval of the Si NMs onto the PDMS stamps, and before their transfer to PLGA, removed any residual photoresist. A field emission SEM (S4800, Hitachi) allowed for high-resolution imaging of the Si NMs.

**In Vitro Dissolution Tests.** Assembly of printed Si NMs was performed on sterilized glass-bottom dishes with a 14 mm well (Cellvis) for long-term cell culture. The culture media consisted of Dulbecco's modified Eagle medium (Thermo-Fisher Scientific), fetal bovine serum (10% v/v; Thermo-Fisher Scientific), and penicillin–streptomycin (1%; Lonza). At different stages of culture, aged samples were rinsed with deionized water and lysed in 0.25% trypsin and 2.21

mM ethylenediaminetetraacetic acid (Corning) to remove cells and stained sediments for profilometry (3030, Dektak; NexView, Zygo), AFM (Cypher, Asylum Research), and XPS (PHI 5400, RBD Instruments) measurements of the time evolution of thicknesses, surface morphologies, and chemical compositions, respectively. Additional extracts were obtained by decanting DPBS (Corning) from the test structure after dissolution of materials of interest, followed by sterile filtration with 0.2 μm in pore size before use. Resulting stock solutions were measured in duplicate wells by ICP-OES (Optima 8300, PerkinElmer) in a clean air room to determine the concentration of Si and W. A mixture of nitric acid (trace metal grade, 67–70%) and hydrochloric acid (trace metal grade, 34–37%) in a ratio of 5:1 was used to initially digest the samples, which were further subjected to an automated sequential microwave digester (Discover SP-D, CEM Corp.) The final clear transparent digest was analyzed by ICP-OES (100 ± 5% accuracy) calibrated based on single-element standards of 1000 ppm concentration (High-Purity Standards). At least two emission lines were observed for the conditioned DPBS, and the one with the highest intensity and lowest relative standard deviation (<1.1%) was used for this study (207.9 nm for W and 212.412 nm for Si). Aliquots of the thick concentrates of conditioned DPBS were added to culture medium in each well for conditioned cell culture.

**Cell Culture and Viability Assay.** CCD18 human colon fibroblasts were seeded at a density of 5000 cells/cm<sup>2</sup> in 12-well plates (Corning) and were precultured in pristine culture media for 5 h prior to conditioned culture. Viable cells were then placed on the test structures with conditioned media and incubated at 37 °C in a humidified atmosphere with 5% CO<sub>2</sub>. Cells were stained with Hoechst 33342 (2 μg/mL; Thermo Scientific), and both phase-contrast and fluorescent images were taken *in situ* before and after conditioned culture, where trypan blue treatment (Sigma-Aldrich) facilitated imaging of cell nuclei for quantitative analysis of live/dead assay. The numbers of viable cells in at least four randomly chosen fields were counted and averaged to yield the final result. We note that another cell line, monkey kidney fibroblasts (MKFs), was also tested to assess tissue cytotoxicity and material bioresorption, which showed no significant difference in material degradation nor adverse effects on the cellular response (although not shown here) compared to the presented CCD18 results.

**In Situ Characterization of Cell–Extracellular Matrix Mechanotransduction.** Test structures for TFM characterization were prepared following the protocol reported by Tse and Engler for synthesis of PA gels on printed NMs/microcomponents.<sup>62</sup> First, sterilized glass-bottom dishes with printed NMs/microcomponents were silanized by (3-aminopropyl)trimethoxysilane (Sigma-Aldrich) and functionalized with glutaraldehyde (0.5%; Polysciences) to facilitate PA gel attachment. A mixture of acrylamide (40%; Sigma-Aldrich), *N,N'*-methylenebisacrylamide (2%; Sigma-Aldrich), and DPBS was then used to generate a liquid PA gel overcoat (modulus of ~5 kPa) on the silanized substrate, followed by ammonium persulfate (1% v/v; Bio-Rad) and tetramethylethylenediamine (0.1% v/v; Bio-Rad) to catalyze the polymerization reaction. To prepare fluorescent beads (100 nm diameter), additional glass coverslips (#1, 12 mm diameter; Ted Pella) treated by poly-D-lysine (0.1 mg/mL; Sigma-Aldrich) for 1 h were blow-dried to support red fluorescent beads (540/600 excitation/emission wavelength in nm) sourced from a colloid suspension (1:5000 diluted, Thermo-Fisher).<sup>63</sup> By placing the processed coverslips onto PA gel-coated samples during gel polymerization, fluorescent beads were uniformly embedded into the liquid PA gel *via* gravity-driven diffusion. After removal of the coverslips, sulfosuccinimidyl-6-(4'-azido-2'-nitrophenylamino)-hexanoate (0.02%; Thermo Scientific) in 4-(2-hydroxyethyl)-1-piperazineethanesulfonic acid (HEPES) buffer (50 mM, pH 8.5; Fisher Scientific) was applied with UV activation to complete the process. The test structures were immersed overnight in a fibronectin solution (human, 25 μg/mL; Corning) in HEPES buffer for protein functionalization and rinsed three times with DPBS before seeding CCD18 fibroblasts. Phase-contrast and fluorescent images of hybrid cells/test structure were obtained for TFM studies after 18 h of

culture. By comparing the fluorescent images before and after culture, traction stress/force and strain energy can be quantified using the following equations: maximum traction stress =  $\max((\tau_x^2 + \tau_y^2)^{1/2})$ , total traction force =  $\int_{\text{cell area}} |(\tau_x^2 + \tau_y^2)^{1/2}| dA$ , and total strain energy =  $(1/2) \int_{\text{cell area}} |(\tau_x d_x + \tau_y d_y)| dA$ , where  $d$  is measured displacement and  $\tau$  is local traction stress around area  $dA$ .<sup>64,65</sup> Analysis of TFM images was performed using ImageJ open-source software.

## ASSOCIATED CONTENT

### Supporting Information

The Supporting Information is available free of charge on the ACS Publications website at DOI: 10.1021/acs.nano.8b04513.

Supporting Figures S1–S3 (PDF)

## AUTHOR INFORMATION

### Corresponding Authors

\*E-mail: saif@illinois.edu.

\*E-mail: jrogers@northwestern.edu.

### ORCID

Jan-Kai Chang: 0000-0002-3056-1250

Chih-I Wu: 0000-0003-3613-7511

John A. Rogers: 0000-0002-2980-3961

### Author Contributions

<sup>†</sup>J.-K. Chang and M. A. Bashar Emon contributed equally to the work.

### Notes

The authors declare no competing financial interest.

## ACKNOWLEDGMENTS

The authors thank the Micro-Nano-Mechanical Systems Laboratory at the University of Illinois at Urbana–Champaign for sample preparation and material characterization. The authors thank Prof. P. Ferreira for the use of transfer printing tools, Dr. K. Subedi for ICP-OES measurement, and Dr. R. Haasch for informative discussions on XPS analysis. This work was supported by the Center for Bio-Integrated Electronics at Northwestern University.

## REFERENCES

- (1) Kang, S. K.; Murphy, R. K.; Hwang, S. W.; Lee, S. M.; Harburg, D. V.; Krueger, N. A.; Shin, J.; Gamble, P.; Cheng, H.; Yu, S.; Liu, Z.; McCall, J.; Stephen, M.; Ying, H.; Kim, J.; Park, G.; Webb, R.; Lee, C.; Chung, S.; Wie, D.; et al. Bioresorbable Silicon Electronic Sensors for the Brain. *Nature* **2016**, *530*, 71–76.
- (2) Yu, K. J.; Kuzum, D.; Hwang, S. W.; Kim, B. H.; Juul, H.; Kim, N. H.; Won, S. M.; Chiang, K.; Trumpis, M.; Richardson, A. G.; Cheng, H.; Fang, H.; Thompson, M.; Bink, H.; Talos, D.; Seo, K. J.; Lee, H. N.; Kang, S. K.; Kim, J.-H.; Lee, J. Y.; et al. Bioresorbable Silicon Electronics for Transient Spatiotemporal Mapping of Electrical Activity from the Cerebral Cortex. *Nat. Mater.* **2016**, *15*, 782–791.
- (3) Curry, E. J.; Ke, K.; Chorsi, M. T.; Wrobel, K. S.; Miller, A. N.; Patel, A.; Kim, I.; Feng, J.; Yue, L.; Wu, Q.; Kuo, C.-L.; Lo, K. W.-H.; Laurencin, C. T.; Horea, L.; Purohit, P. K.; Nguyen, T. D. Biodegradable Piezoelectric Force Sensor. *Proc. Natl. Acad. Sci. U. S. A.* **2018**, *115*, 201710874.
- (4) Lacour, S. P.; Courtine, G.; Guck, J. Materials and Technologies for Soft Implantable Neuroprostheses. *Nat. Rev. Mater.* **2016**, *1*, 16063.
- (5) Someya, T.; Bao, Z.; Malliaras, G. G. The Rise of Plastic Bioelectronics. *Nature* **2016**, *540*, 379–385.

(6) Tan, M. J.; Owh, C.; Chee, P. L.; Kyaw, A. K. K.; Kai, D.; Loh, X. J. Biodegradable Electronics: Cornerstone for Sustainable Electronics and Transient Applications. *J. Mater. Chem. C* **2016**, *4*, 5531–5558.

(7) Hwang, S. W.; Tao, H.; Kim, D.-H.; Cheng, H.; Song, J.-K.; Rill, E.; Brenckle, M. A.; Panilaitis, B.; Won, S. M.; Kim, Y.-S.; Song, Y. M.; Yu, K. J.; Ameen, A.; Li, R.; Su, Y.; Yang, M.; Kaplan, D. L.; Zakin, M. R.; Slepian, M. J.; Huang, Y.; Omenetto, F. G.; Rogers, J. A. A Physically Transient Form of Silicon Electronics. *Science* **2012**, *337*, 1640–1644.

(8) Lee, Y. K.; Yu, K. J.; Song, E.; Barati Farimani, A.; Vitale, F.; Xie, Z.; Yoon, Y.; Kim, Y.; Richardson, A.; Luan, H.; Wu, Y.; Xie, X.; Lucas, T. H.; Crawford, K.; Mei, Y.; Feng, X.; Huang, Y.; Litt, B.; Aluru, N. R.; Yin, L.; Roger, J. A. Dissolution of Monocrystalline Silicon Nanomembranes and Their Use as Encapsulation Layers and Electrical Interfaces in Water-Soluble Electronics. *ACS Nano* **2017**, *11*, 12562–12572.

(9) Aguado, B. A.; Grim, J. C.; Rosales, A. M.; Watson-Capps, J. J.; Anseth, K. S. Engineering Precision Biomaterials for Personalized Medicine. *Sci. Transl. Med.* **2018**, *10*, eaam8645.

(10) Shou, W.; Mahajan, B. K.; Ludwig, B.; Yu, X.; Staggs, J.; Huang, X.; Pan, H. Low-Cost Manufacturing of Bioresorbable Conductors by Evaporation–Condensation-Mediated Laser Printing and Sintering of Zn Nanoparticles. *Adv. Mater.* **2017**, *29*, 1700172.

(11) Aigner, T. B.; DeSimone, E.; Scheibel, T. Biomedical Applications of Recombinant Silk-Based Materials. *Adv. Mater.* **2018**, *30*, 1704636.

(12) Chen, C.; Zhang, Y.; Li, Y.; Dai, J.; Song, J.; Yao, Y.; Gong, Y.; Kierzewski, I.; Xie, J.; Hu, L. All-Wood, Low Tortuosity, Aqueous, Biodegradable Supercapacitors with Ultra-High Capacitance. *Energy Environ. Sci.* **2017**, *10*, 538–545.

(13) Kang, S.-K.; Hwang, S.-W.; Cheng, H.; Yu, S.; Kim, B. H.; Kim, J.-H.; Huang, Y.; Rogers, J. A. Dissolution Behaviors and Applications of Silicon Oxides and Nitrides in Transient Electronics. *Adv. Funct. Mater.* **2014**, *24*, 4427–4434.

(14) Chang, J.-K.; Fang, H.; Bower, C. A.; Song, E.; Yu, X.; Rogers, J. A. Materials and Processing Approaches for Foundry-Compatible Transient Electronics. *Proc. Natl. Acad. Sci. U. S. A.* **2017**, *114*, E5522–E5529.

(15) Hwang, S.-W.; Kim, D.-H.; Tao, H.; Kim, T.-I.; Kim, S.; Yu, K. J.; Panilaitis, B.; Jeong, J.-W.; Song, J.-K.; Omenetto, F. G.; Rogers, J. A. Materials and Fabrication Processes for Transient and Bioresorbable High-Performance Electronics. *Adv. Funct. Mater.* **2013**, *23*, 4087–4093.

(16) Tao, H.; Hwang, S.-W.; Marelli, B.; An, B.; Moreau, J. E.; Yang, M.; Brenckle, M. A.; Kim, S.; Kaplan, D. L.; Rogers, J. A.; Omenetto, F. G. Silk-Based Resorbable Electronic Devices for Remotely Controlled Therapy and in Vivo Infection Abatement. *Proc. Natl. Acad. Sci. U. S. A.* **2014**, *111*, 17385–17389.

(17) Park, J.-H.; Gu, L.; Maltzahn, G. V.; Ruoslahti, E.; Bhatia, S. N.; Sailor, M. J. Biodegradable Luminescent Porous Silicon Nanoparticles for in Vivo Applications. *Nat. Mater.* **2009**, *8*, 331–336.

(18) Chen, L. Y.; Tee, B. C.-K.; Chortos, A. L.; Schwartz, G.; Tse, V.; Lipomi, D. J.; Wong, H.-S. P.; McConnell, M. V.; Bao, Z. Continuous Wireless Pressure Monitoring and Mapping with Ultra-Small Passive Sensors for Health Monitoring and Critical Care. *Nat. Commun.* **2014**, *5*, 5028.

(19) Moghimi, S. M.; Hunter, A. C.; Murray, J. C. Nanomedicine: Current Status and Future Prospects. *FASEB J.* **2005**, *19*, 311–330.

(20) Mitragotri, S.; Lahann, J. Physical Approaches to Biomaterial Design. *Nat. Mater.* **2009**, *8*, 15–23.

(21) Bayliss, S. C.; Heald, R.; Fletcher, D. I.; Buckberry, L. D. The Culture of Mammalian Cells on Nanostructured Silicon. *Adv. Mater.* **1999**, *11*, 318–321.

(22) Dalilottojari, A.; Tong, W. Y.; McInnes, S. J.; Voelcker, N. H. Biocompatibility and Bioactivity of Porous Silicon. In *Porous Silicon: From Formation to Application*; CRC Press, Taylor & Francis Group: Boca Raton, 2016; pp 319–335.

- (23) Jaganathan, H.; Godin, B. Biocompatibility Assessment of Si-Based Nano- and Micro-Particles. *Adv. Drug Delivery Rev.* **2012**, *64*, 1800–1819.
- (24) Curtis, A.; Wilkinson, C. Topographical Control of Cells. *Biomaterials* **1997**, *18*, 1573–1583.
- (25) Bayliss, S. C.; Buckberry, L. D.; Harris, P. J.; Tobin, M. Nature of the Silicon-Animal Cell Interface. *J. Porous Mater.* **2000**, *7*, 191–195.
- (26) Kang, S.-K.; Park, G.; Kim, K.; Hwang, S.-W.; Cheng, H.; Shin, J.; Chung, S.; Kim, M.; Yin, L.; Lee, J. C.; Lee, K.-M.; Rogers, J. A. Dissolution Chemistry and Biocompatibility of Silicon- and Germanium-Based Semiconductors for Transient Electronics. *ACS Appl. Mater. Interfaces* **2015**, *7*, 9297–9305.
- (27) Hwang, S.-W.; Park, G.; Edwards, C.; Corbin, E. A.; Kang, S.-K.; Cheng, H.; Song, J.-K.; Kim, J.-H.; Yu, S.; Ng, J.; Lee, J. E.; Kim, J.; Yee, C.; Bhaduri, B.; Su, Y.; Omennetto, F. G.; Huang, Y.; Bashir, R.; Goddard, L.; Popescu, G.; et al. Dissolution Chemistry and Biocompatibility of Single-Crystalline Silicon Nanomembranes and Associated Materials for Transient Electronics. *ACS Nano* **2014**, *8*, 5843–5851.
- (28) Bayliss, S. C.; Buckberry, L. D.; Fletcher, I.; Tobin, M. J. The Culture of Neurons on Silicon. *Sens. Actuators, A* **1999**, *74*, 139–142.
- (29) Yin, L.; Farimani, A. B.; Min, K.; Vishal, N.; Lam, J.; Lee, Y. K.; Aluru, N. R.; Rogers, J. A. Silicon Nanomembranes: Mechanisms for Hydrolysis of Silicon Nanomembranes as Used in Bioresorbable Electronics. *Adv. Mater.* **2015**, *27*, 1856–1856.
- (30) Low, S. P.; Voelcker, N. H. Biocompatibility of Porous Silicon. In *Handbook of Porous Silicon*; Canham, L. T., Ed.; Springer International Publishing: Cham, Switzerland, 2014; pp 381–393.
- (31) Raven, J. A. The Transport and Function of Silicon in Plants. *Biol. Rev.* **1983**, *58*, 179–207.
- (32) Maiorano, G.; Sabella, S.; Sorce, B.; Brunetti, V.; Malvindi, M. A.; Cingolani, R.; Pompa, P. P. Effects of Cell Culture Media on the Dynamic Formation of Protein–Nanoparticle Complexes and Influence on the Cellular Response. *ACS Nano* **2010**, *4*, 7481–7491.
- (33) Arora, M. Cell Culture Media: A Review. *Mater. Methods* **2013**, *3*, 175.
- (34) Anderson, I. W. The Cambridge Prize Lecture 1995: Indirect and Direct Contributions of Barley Malt to Brewing. *J. Inst. Brew.* **1996**, *102*, 409–413.
- (35) Wainwright, M.; Al-Wajeeh, K.; Grayston, S. J. Effect of Silicic Acid and Other Silicon Compounds on Fungal Growth in Oligotrophic and Nutrient-Rich Media. *Mycol. Res.* **1997**, *101*, 933–938.
- (36) Icopini, G. A.; Brantley, S. L.; Heaney, P. J. Kinetics of Silica Oligomerization and Nanocolloid Formation as a Function of pH and Ionic Strength at 25 C. *Geochim. Cosmochim. Acta* **2005**, *69*, 293–303.
- (37) Belton, D. J.; Deschaume, O.; Perry, C. C. An Overview of the Fundamentals of the Chemistry of Silica with Relevance to Biosilicification and Technological Advances. *FEBS J.* **2012**, *279*, 1710–1720.
- (38) Gunda, N. S. K.; Singh, M.; Norman, L.; Kaur, K.; Mitra, S. K. Optimization and Characterization of Biomolecule Immobilization on Silicon Substrates Using (3-Aminopropyl)Triethoxysilane (APTES) and Glutaraldehyde Linker. *Appl. Surf. Sci.* **2014**, *305*, 522–530.
- (39) Lavagnino, M.; Arnoczky, S. P. Vitro Alterations in Cytoskeletal Tensional Homeostasis Control Gene Expression in Tendon Cells. *J. Orthop. Res.* **2005**, *23*, 1211–1218.
- (40) Arnoczky, S. P.; Lavagnino, M.; Egerbacher, M.; Caballero, O.; Gardner, K.; Shender, M. A. Loss of Homeostatic Strain Alters Mechanostat “Set Point” of Tendon Cells in Vitro. *Clin. Orthop. Relat. Res.* **2008**, *466*, 1583–1591.
- (41) Wang, J. H. C.; Li, B. Application of Cell Traction Force Microscopy for Cell Biology Research. *Methods Mol. Biol.* **2009**, *586*, 301–313.
- (42) Holle, A. W.; Young, J. L.; Vliet, K. J. V.; Kamm, R. D.; Discher, D.; Janmey, P.; Spatz, J. P.; Saif, T. Cell–Extracellular Matrix Mechanobiology: Forceful Tools and Emerging Needs for Basic and Translational Research. *Nano Lett.* **2018**, *18*, 1–8.
- (43) Carlisle, E. M. Silicon: an Essential Element for the Chick. *Science* **1972**, *178*, 619–621.
- (44) Carlisle, E. M. The Nutritional Essentiality of Silicon. *Nutr. Rev.* **1982**, *40*, 193–198.
- (45) Mayne, A.; Bayliss, S.; Barr, P.; Tobin, M.; Buckberry, L. Biologically Interfaced Porous Silicon Devices. *Phys. Status Solidi A* **2000**, *182*, 505–513.
- (46) Agrawal, A.; Nehilla, B.; Reisig, K.; Gaborski, T.; Fang, D.; Striemer, C.; Fauchet, P.; Mcgrath, J. Porous Nanocrystalline Silicon Membranes as Highly Permeable and Molecularly Thin Substrates for Cell Culture. *Biomaterials* **2010**, *31*, 5408–5417.
- (47) Karaman, D. Ş.; Sarparanta, M. P.; Rosenholm, J. M.; Airaksinen, A. J. Multimodality Imaging of Silica and Silicon Materials in Vivo. *Adv. Mater.* **2018**, *30*, 1703651.
- (48) Witten, M. L.; Sheppard, P. R.; Witten, B. L. Tungsten Toxicity. *Chem.-Biol. Interact.* **2012**, *196*, 87–88.
- (49) Mcinturf, S.; Bekkedal, M.; Wilfong, E.; Arfsten, D.; Chapman, G.; Gunasekar, P. The Potential Reproductive, Neurobehavioral and Systemic Effects of Soluble Sodium Tungstate Exposure in Sprague–Dawley Rats. *Toxicol. Appl. Pharmacol.* **2011**, *254*, 133–137.
- (50) Kalinich, J. F.; Emond, C. A.; Dalton, T. K.; Mog, S. R.; Coleman, G. D.; Kordell, J. E.; Miller, A. C.; McClain, D. E. Embedded Weapons-Grade Tungsten Alloy Shrapnel Rapidly Induces Metastatic High-Grade Rhabdomyosarcomas in F344 Rats. *Environ. Health Perspect.* **2005**, *113*, 729–734.
- (51) Chen, Q.; Thouas, G. Metallic Implant Biomaterials. *Mater. Sci. Eng., R* **2015**, *87*, 1–57.
- (52) Peuster, M.; Fink, C.; von Schnakenburg, C. Biocompatibility of Corroding Tungsten Coils: in Vitro Assessment of Degradation Kinetics and Cytotoxicity on Human Cells. *Biomaterials* **2003**, *24*, 4057–4061.
- (53) Lison, D.; Bucket, J. P.; Hoet, P. Toxicity of Tungsten. *Lancet* **1997**, *349*, 58–59.
- (54) Peuster, M.; Fink, C.; Schnakenburg, C. V.; Hausdorf, G. Dissolution of Tungsten Coils Does Not Produce Systemic Toxicity, but Leads to Elevated Levels of Tungsten in the Serum and Recanalization of the Previously Occluded Vessel. *Cardiol. Young* **2002**, *12*, 229–235.
- (55) Yin, L.; Cheng, H.; Mao, S.; Haasch, R.; Liu, Y.; Xie, X.; Hwang, S.-W.; Jain, H.; Kang, S.-K.; Su, Y.; Li, R.; Huang, Y.; Rogers, J. A. Transient Electronics: Dissolvable Metals for Transient Electronics. *Adv. Funct. Mater.* **2014**, *24*, 645–658.
- (56) Lee, Y. K.; Yu, K. J.; Kim, Y.; Yoon, Y.; Xie, Z.; Song, E.; Luan, H.; Feng, X.; Huang, Y.; Rogers, J. A. Kinetics and Chemistry of Hydrolysis of Ultrathin, Thermally Grown Layers of Silicon Oxide as Biofluid Barriers in Flexible Electronic Systems. *ACS Appl. Mater. Interfaces* **2017**, *9*, 42633–42638.
- (57) Chang, J.-K.; Chang, H.-P.; Guo, Q.; Koo, J.; Wu, C.-I.; Rogers, J. A. Flexible Electronics: Biodegradable Electronic Systems in 3D, Heterogeneously Integrated Formats. *Adv. Mater.* **2018**, *30*, 1870077.
- (58) van Hove, R. P.; Siersevelt, I. N.; van Royen, B. J.; Nolte, P. A. Titanium-Nitride Coating of Orthopaedic Implants: A Review of the Literature. *BioMed Res. Int.* **2015**, *2015*, 485975.
- (59) Yaghoubi, S.; Schwietert, C. W.; McCue, J. P. Biological Roles of Titanium. *Biol. Trace Elem. Res.* **2000**, *78*, 205–217.
- (60) Lee, S.; Kang, B.; Keum, H.; Ahmed, N.; Rogers, J. A.; Ferreira, P. M.; Kim, S.; Min, B. Heterogeneously Assembled Metamaterials and Metadevices via 3D Modular Transfer Printing. *Sci. Rep.* **2016**, *6*, 27621.
- (61) Qin, D.; Xia, Y.; Whitesides, G. M. Soft Lithography for Micro- and Nanoscale Patterning. *Nat. Protoc.* **2010**, *5*, 491.
- (62) Tse, J. R.; Engler, A. J. Preparation of Hydrogel Substrates with Tunable Mechanical Properties. *Curr. Protoc. Cell Biol.* **2010**, *47*, 10–16.
- (63) Knoll, S. G.; Ali, M. K.; Saif, M. T. A. A Novel Method for Localizing Reporter Fluorescent Beads near the Cell Culture Surface for Traction Force Microscopy. *J. Visualized Exp.* **2014**, *91*, 51873.
- (64) Wang, J. H.; Lin, J. S. Cell Traction Force and Measurement Methods. *Biomech. Model. Mechanobiol.* **2007**, *6*, 361.

(65) Butler, J. P.; Tolic-Nørrelykke, I. M.; Fabry, B.; Fredberg, J. J. Traction Fields, Moments, and Strain Energy that Cells Exert on Their Surroundings. *Am. J. Physiol. Cell Physiol.* **2002**, *282*, C595–C605.